UC Berkeley

UC Berkeley Previously Published Works

Title

Boron-Doped Graphene Nanoribbons: Electronic Structure and Raman Fingerprint

Permalink

https://escholarship.org/uc/item/7mm8q9fr

Journal

ACS Nano, 12(8)

ISSN

1936-0851

Authors

Senkovskiy, Boris V
Usachov, Dmitry Yu
Fedorov, Alexander V
et al.

Publication Date

2018-08-28

DOI

10.1021/acsnano.8b04125

Peer reviewed

eScholarship.org Powered by the California Digital Library
University of California

Boron-Doped Graphene Nanoribbons: Electronic Structure and Raman Fingerprint

Boris V. Senkovskiy,[*,†] Dmitry Yu. Usachov,[‡] Alexander V. Fedorov,[†,‡,¶] Tomas Marangoni,[§] Danny Haberer,[§] Cesare Tresca,[‖,⊥] Gianni Profeta,[‖] Vasile Caciuc,[#] Shigeru Tsukamoto,[#] Nicolae Atodiresei,[#] Niels Ehlen,[†] Chaoyu Chen,[@] José Avila,[@] Maria C. Asensio,[@] Andrei Varykhalov,[△] Alexei Nefedov,[▽] Christof Wöll,[▽] Timur K. Kim,[††] Moritz Hoesch,[††] Felix R. Fischer,[§,‡‡,¶¶] and Alexander Grüneis[*,†]

†*II. Physikalisches Institut, Universität zu Köln, Zülpicher Strasse 77, 50937 Köln, Germany*

‡*St. Petersburg State University, 7/9 Universitetskaya nab., St. Petersburg, 199034, Russia*

¶*IFW Dresden, P.O. Box 270116, Dresden D-01171, Germany*

§*Department of Chemistry, University of California at Berkeley, Tan Hall 680, Berkeley, CA 94720, USA*

‖*Department of Physical and Chemical Sciences and SPIN-CNR, University of L'Aquila , Via Vetoio 10, I-67100 Coppito, Italy*

⊥*Institut des Nanosciences de Paris, Sorbonne Universités-UPMC univ Paris 6 and CNRS-UMR 7588, 4 place Jussieu, F-75252 Paris, France*

#*Peter Grünberg Institut (PGI-1) and Institute for Advanced Simulation (IAS-1), Forschungszentrum Jülich and JARA, D-52425 Jülich, Germany*

@*ANTARES Beamline, Synchrotron SOLEIL & Universite Paris-Saclay, L' Orme des Merisiers, Saint Aubin-BP 48, 91192 Gif sur Yvette Cedex, France*

△*Helmholtz-Zentrum Berlin für Materialien und Energie, Berlin, Germany*

▽*Institut für Funktionelle Grenzflächen (IFG), Karlsruher Institut für Technologie (KIT), Hermann-von-Helmholtz-Platz 1, 76344 Eggenstein-Leopoldshafen, Germany*

††*Diamond Light Source, Harwell Campus, Didcot, OX11 0DE, United Kingdom*

‡‡*Materials Science Division, Lawrence Berkeley National Laboratory, Berkeley, California 94720, United States*

¶¶*Kavli Energy Nanosciences Institute at the University of California Berkeley and Lawrence Berkeley National Laboratory, Berkeley, California 94720, United States*

E-mail: senkovskiy@ph2.uni-koeln.de; grueneis@ph2.uni-koeln.de

Abstract

We investigate the electronic and vibrational properties of bottom-up synthesized aligned armchair graphene nanoribbons of $N = 7$ carbon atoms width periodically doped by substitutional boron atoms (B-7AGNRs). Using angle-resolved photoemission spectroscopy (ARPES) and density functional theory (DFT) calculations, we find that the dopant-derived valence and conduction band states are notably hybridized with electronic states of Au substrate and spread in energy. The interaction with the substrate leaves the bands with pure carbon character rather unperturbed. This results in an identical effective mass of $\sim 0.2\ m_0$ for the next highest valence band compared to pristine 7AGNRs. We probe the phonons of B-7AGNRs *in situ* by Raman spectroscopy and reveal the existence of characteristic splittings and red-shifts of Raman modes due to the presence of substitutional boron atoms. Comparing the Raman spectra for three visible lasers (red, green and blue) we find that interaction with gold suppresses the Raman signal from B-7AGNRs and the energy of a green laser (2.33 eV) is closer to the resonant E_{22} transition. The hybridized electronic structure of the B-7AGNR/Au interface is expected to improve electrical characteristics of contacts between graphene nanoribbon and Au. The Raman fingerprint allows easy identification of B-7AGNRs, that is particularly useful for device fabrication.

KEYWORDS: graphene nanoribbons, boron doping, electronic structure, ARPES, Raman, substrate interaction

Doping a semiconductor by foreign atoms of a different valency is a means to shift the chemical potential and to engineer the carrier concentration providing the basis for modern electronic devices. Semiconducting graphene nanoribbons (GNRs) have a great potential for nanoelectronics and optics, since their structure can be engineered with atomic precision by bottom-up synthesis from molecular precursors and their electronic band structure can be tuned in a wide range.[1–7] Recently, the incorporation of boron atoms, acting as p-type dopants, into the lattice of armchair graphene nanoribbons of N=7 carbon atoms width (7AGNRs) has been demonstrated.[8,9] The pairs of boron atoms in the synthesized B-

7AGNRs are periodically embedded in the carbon backbones at defined positions, forming a superstructure along the ribbon axis. The atomically precise control of the dopant positions in the crystal structure of GNRs is an exceptional case. For example, the sublattice specific incorporation of boron in epitaxial graphene has been demonstrated,[10] but it by far lacks perfection that can be achieved by bottom-up nanotechnology. Indeed, if dopant atoms occupy random positions of the graphene lattice, the perturbations in periodic potential contribute to the momentum scattering of charge carriers limiting the electron mobility.[11] However, if heteroatoms are periodically incorporated in the crystal, translational symmetry is preserved and hence the momentum is conserved.[12,13] This clearly should improve transport characteristics of B-doped GNRs, which are very interesting for technological applications as gas sensors, solar cell components or electrocatalysts.[9,14,15] Heterojunctions of pristine and B-doped 7AGNRs attract attention in the context of electronic transport.[16] It has also been predicted theoretically, that B-doped and pristine 7AGNRs belong to the different topological classes.[17] Because of this, pristine and doped segments fused together exhibit localized junction states with tunable magnetic coupling.[17] Therefore, it is mandatory for the field to unambiguously determine the energy band structure of B-doped GNRs.

Intuitively, one expects that the incorporation of boron atoms (having one electron less than the carbon host) results in hole doping. The periodicity of boron is expected to lead to the formation of valence and conduction bands with significant boron contribution to the density of states and a weak dispersion. Such bands were predicted in B-7AGNRs by *ab initio* calculations.[8,17] However, there is no clear observation of these bands by scanning tunneling spectroscopy (STS). Indeed, the STS measurements of B-doped 7AGNRs on Au(111) surprisingly reveal the same value of quasiparticle band gap as for the pristine system – 2.4 eV.[9] Theory based on GW approximation (which include screening of the electron-electron interaction by a metal substrate) predicts the energy separation between the dopant-derived bands in B-7AGNRs of only 0.8 eV,[8] which is much less than the value measured by STS.[9] The discrepancy may be due to the fact that in realistic systems, B-7AGNR electronic band

structure is affected by the substrate. This influence has not been studied in Refs. 8,9. Moreover, there are no measurements of the electron energy dispersion relation of B-7AGNRs. To shed light on these questions we synthesized aligned B-7AGNRs on a stepped Au(788) crystal with (111) terraces (see Methods section) to measure the energy band dispersion of B-7AGNR using angle-resolved photoemission spectroscopy (ARPES).

For further progress in creation of GNR-based devices[18–21] an important task is to identify the type and orientation of GNRs on both growth metallic and on insulating substrates. In this respect, the most promising fingerprinting method is Raman spectroscopy, which has been applied to characterize GNRs of numerous types.[1,5,6,22–27] Until now, however, it is not clear how periodic boron doping affects the Raman spectra of GNRs. Yet is is clear that atomically precise functionalization with heteroatoms and edge groups is an effective route to tune the electronic and vibrational properties of GNRs.[8,9,28–40] The present work addresses this issue by a detailed experimental investigation of B-7AGNRs using *in situ* ultra-high vacuum (UHV) Raman spectroscopy to unravel the changes in vibrational properties of 7AGNRs induced by the periodically incorporated B atoms. We also compare the Raman spectra of pristine and B-doped 7AGNRs with different laser energies to explore the optical resonance transitions. Our studies are supported by X-ray photoelectron and absorption spectroscopies as well as by density functional theory (DFT) calculations of the electronic and vibrational properties.

Results and Discussion

Stoichiometry and corrugation

Aligned B-7AGNRs were synthesized on vicinal Au(788) crystal with narrow (111) terraces using a similar recipe previously applied for synthesis on Au(111)[8,9] (see Methods section). The alignment is needed for ARPES and polarized Raman measurements, discussed in the following sections. The chemical state, composition and the structure of synthesized

B-7AGNRs were probed by X-ray photoelectron spectroscopy (XPS) and near-edge X-ray absorption fine structure (NEXAFS) spectroscopy. Figure 1 (a) illustrates different chemical environments of carbon atoms present in B-7AGNRs. There are C atoms surrounded by three other C atoms (denoted as C_1) or having only two C neighbours and either H or B as a third neighbour (C_2 and C_3, respectively). Figure 1 (b) depicts XPS spectra of B-7AGNRs in the regions of C 1s and B 1s core-levels. The C_1 component's energy is 284.05 eV, which is $\sim$ 0.15 eV smaller than for pristine 7AGNRs.[41] The C_2 component appears at 283.90 eV and the C_3 component at 283.00 eV. A peak similar to the C_3 low energy component was also observed in the B-doped epitaxial graphene.[42] From the components areas we obtain an intact B/C ratio of 1/20 that is expected on the basis of the structure. The B 1s peak consists of one component at 186.8 eV. When B-doped GNRs are affected by air, they are rapidly oxidized and the B 1s peak splits into two components (see Fig. S1 in supplementary information). The high chemical reactivity of the boron sites is consistent with previous studies of boron doped graphene sensors[43] and is highly relevant for the substrate interaction effects as we will show later.

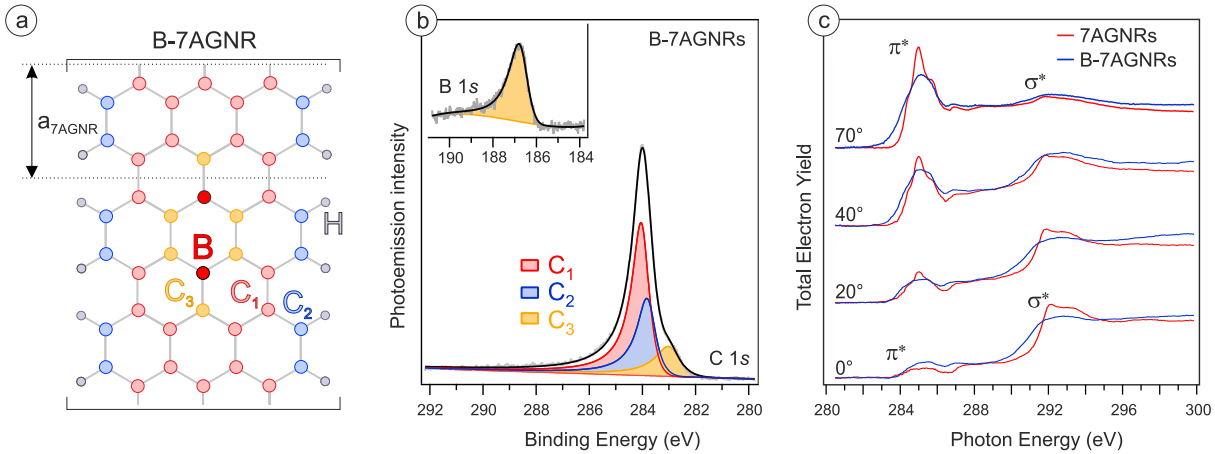

Figure 1: (a) Unit cell of hydrogen-terminated B-7AGNR containing C atoms surrounded by three other C atoms (C_1), C atoms next to an H atom (C_2) and next to a B atom (C_3). The lattice parameter of pristine 7AGNRs is marked as a_{7AGNR}. (b) XPS spectra of the C 1s and the B 1s core levels of B-7AGNRs/Au(788). The C 1s spectrum consists of three components (C_1 – C_3) which correspond to the different chemical environment of C atoms. (c) Comparison of the C K-edge NEXAFS spectra of pristine and B-doped 7AGNRs on Au(788) at different angles between the light polarization vector and the sample surface.

Let us now look at the C K-edge NEXAFS spectra which are related to the transitions from the C 1s core levels to unoccupied π^* and σ^* states. According to the selection rules for X-ray absorption, the π^* (σ^*) resonance should be suppressed (enhanced) when the incident light is polarized along the flat sheet of sp^2 bonded carbon and enhanced (suppressed) when the light has out-of-plane polarization. Comparing the spectra of pristine and B-doped 7AGNRs in Figure 1 (c), one can find that in B-7AGNRs for normal incidence of linearly polarized radiation (0°) the π^* resonance has a higher intensity and the σ^* resonance has a lower intensity with respect to the 7AGNRs. Based on the angular dependence of the matrix element, this behavior suggests that, unlike to the pristine system, B-7AGNRs have out-of-plane corrugations on the Au substrate. This observation confirms that one of the reasons of a frequency shift detected in atomic force microscopy experiments when the tip was placed upon a borylated segments[9] is the corrugation of B-7AGNRs on Au(111).

Interestingly, in B-7AGNRs a new contribution to the π^* resonance is rising below 284 eV with increasing angle and becoming most pronounced for grazing incidence (70°). This low energy shoulder is associated with the C_3 atoms having lowest binding energy. Its disappearance at 0° suggests that the out-of-plane structural distortion is mainly related to the C_1 and C_2 atoms. This may be if the B atoms are pulling the nearest neighbour carbons towards the Au surface forcing the rest nanoribbon structure to buckle. The interaction of B sites with the substrate should affect the electronic band structure of B-7AGNRs.

Electronic band structure

We have recently demonstrated that ARPES mapping of the full two-dimensional (2D) momentum space is needed to visualize and unambiguously determine all valence bands of GNRs.[44] In the following we apply this approach to reveal the electronic energy band structure of B-7AGNRs. Here we consider the 2D in-plane momentum of emitted photoelectrons regarding the ribbons' alignment direction, that is parallel ($k_\parallel$) and perpendicular ($k_\perp$) to the ribbon axis. The parallel component ($k_\parallel$) represents the electron momentum inside the ribbon.

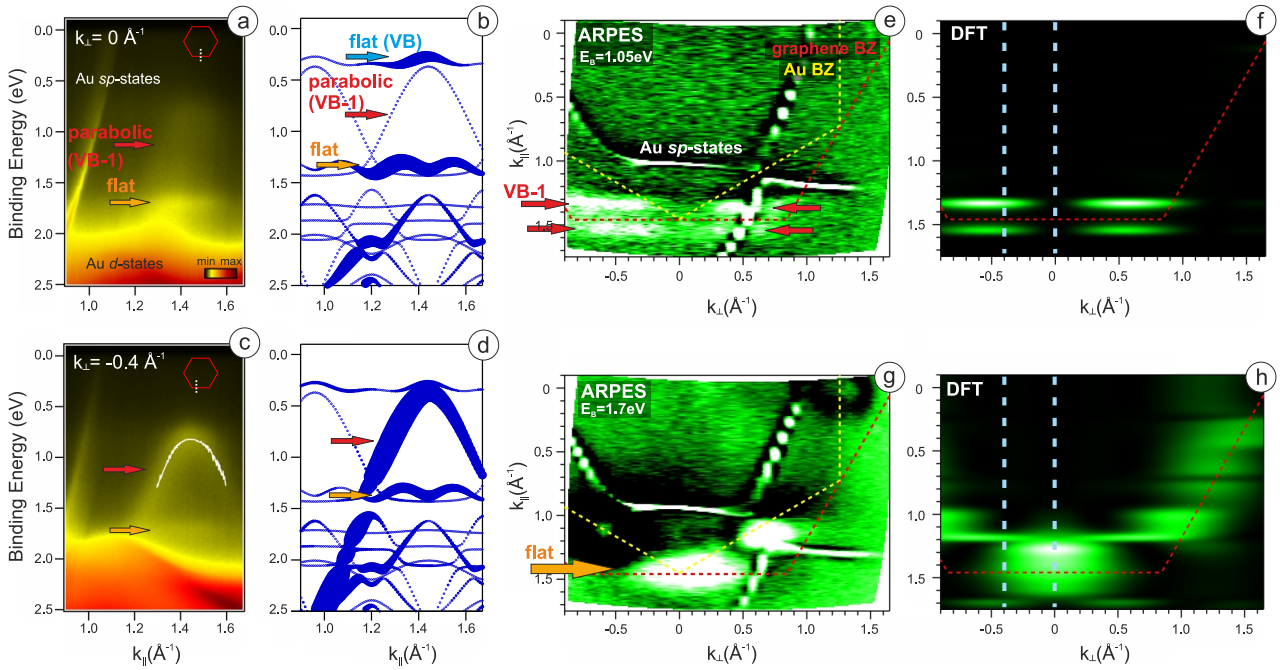

Figure 2: (a) ARPES scan of B-7AGNRs/Au(788) along $k_{\parallel}$ at $k_{\perp} = 0$. The red and orange arrows in the panel (a) indicate the parabolic VB–1 and the low energy flat band of B-7AGNRs, respectively. (b) Calculated photoemission intensity of the carbon π-states of freestanding B-7AGNR for $k_{\perp} = 0$ Å^{-1}. The blue, red and orange arrows indicate the flat VB, parabolic VB–1 and low energy flat band, respectively. (c, d) Similar as for (a, b) but at $k_{\perp} = -0.4$ Å^{-1}. The insets in the upper right corner of the panels (a) and (c) indicate the scan paths (white dashed vertical lines) relative to the BZ of graphene (red hexagon). The white curve in panel (c) indicates the fit of EDCs for VB–1. (e) ARPES map at binding energy of 1.05 eV and (f) the corresponding DFT-calculated map. The red dashed line denotes the BZ edge of 2D graphene and the yellow dashed line denotes BZ edge of Au(111). Regions of high photoemission intensity coming from the parabolic band are indicated by red arrows in panel (e). (g, h) Similar as for (e, f) but at binding energy of 1.7 eV. The photoemission intensity coming from the flat band is indicated by the orange arrow in panel (g). The blue vertical dashed lines in (f) and (h) indicate the direction of the ARPES cuts shown in (a, c). The experimental ARPES maps represent the second derivatives of the intensity by energy to enhance the contrast.

Figure 2 (a) shows an ARPES scan of B-7AGNRs/Au(788) accumulated along $k_{\parallel}$ at constant $k_{\perp} = 0$ Å^{-1}. The scan path relative to the 2D graphene Brillouin zone (BZ) is shown as an inset in the upper right corner of the figure. This scan reveals two nanoribbon-derived electronic states: a flat band at 1.71 eV (marked by an orange arrow in Fig. 2 (a)) and a faint parabolic band (marked by a red arrow), which is the second valence band (VB–1) of B-7AGNRs, as we will see later. Here and in the following we count the first and the second valence bands in the order of their increasing energy offset from the Fermi level and label them as VB and VB–1, respectively. Figure 2 (b) shows the corresponding DFT calculations carried out for freestanding B-7AGNRs (see Methods section). Here the energy is taken as zero (Fermi level) in the center of the band gap. The thickness of the bands in Figure 2 (b) reflects the simulated photoemission intensity at $k_{\perp} = 0$ Å^{-1}. These intensity simulations are similar to what has been done by us for 7-AGNRs, where we constructed a dipole matrix element for the transition between the initial and the plane wave final states.[44] For the initial states of B-7AGNRs we use the DFT-derived wave functions (see Methods sections for details). From the calculations we obtain that those bands of B-7AGNRs that have sufficiently large photoemission intensity are centered at approximately the edge of graphene BZ ($k_{\parallel} = 1.47$ Å^{-1}). Assuming no bond-length change, the unit cell of B-7AGNRs is equal to 3 times the size of the unit cell of 7AGNRs (Fig. 1 (a)). Thus the measured bands belong to the fourth 1D BZ of B-7AGNRs. Particularly, as seen in Figure 2 (b), two weakly dispersing (flat) bands should be observed at $k_{\perp} = 0$ Å^{-1} according to the calculations. The highest one (VB) is marked by a blue arrow and the low-energy flat band by an orange arrow. Importantly, the second valence band (VB-1) with parabolic dispersion indicated by the red arrow is predicted to have much weaker ARPES intensity at this $k_{\perp}$. Comparing the experiment to the calculations (Fig. 2 (a) and (b)), we find agreement for the energetically lower flat band and the low-intensity parabolic band. ARPES does not reveal the theoretically predicted VB close to the Fermi energy, marked by a blue arrow in Figure 2 (b). Previous STS measurements of B-7AGNRs on Au(111) also did not identify

this band.[8,9] The fact that this dopant-derived band is not detectable in experiments is a hint towards its hybridization with the electronic states of Au substrate. We will treat this effect in detail in the following section.

Let us now perform a similar analysis as the one displayed in Figures 2 (a) and (b) for a different value of $k_\perp$ in order to change the intensity of bands. Figure 2 (c) depicts an ARPES scan at $k_\perp = -0.4$ Å^{-1}. The change in $k_\perp$ results in the parabolic band becoming more intense while the flat band becomes weaker. Again, the higher (lower) ARPES intensity of the parabolic (flat) band for $k_\perp = -0.4$ Å^{-1} is nicely reproduced by our ARPES intensity calculations as can be seen in Figure 2 (d). This allows us to perform a detailed analysis of the band parameters. Fit of the ARPES maxima along the energy dispersion curves (EDCs) is indicated by the white curve in Figure 2 (c). We extract the energy of the parabolic band maximum at 0.82 eV and the effective carrier mass of $m^* \sim 0.2\ m_e$ (here m_e is the free electron mass). Note, that the position of this band is very close to the energy of valence band edge at 0.8 eV, measured by STS for B-7AGNRs on Au(111).[9]

The distribution of photoemission intensity of GNRs in the 2D k-space is determined by the electron wave function of the particular band.[26,44] Therefore the full 2D ARPES maps are required to unambiguously assign the experimentally observed valence bands to the calculated band structure. Figure 2 (e) depicts a slice of the ARPES map of the B-7AGNR/Au(788) system at the constant binding energy of 1.05 eV. The red arrows point out the positions in k-space where the parabolic band VB–1 crosses the equi-energy contour. The corresponding DFT calculated map (for freestanding B-7AGNRs) is shown in Figure 2 (f), and it can be seen that the agreement is very good. Two vertical dashed lines of a blue color in Figure 2 (f) correspond to values of $k_\perp = 0$ and $k_\perp = -0.4$ Å^{-1}, which we used for the ARPES measurements shown in Figure 2 (a, c). Figure 2 (g) depicts experimental constant energy maps of ARPES intensity at 1.7 eV. At this energy, the weakly-dispersing band, indicated by the orange arrow in Figure 2 (g), has a maximum intensity. Similarly, the agreement to the calculated ARPES intensity, shown in Figure 2 (h), is good. Thus the

combination of ARPES experiment and simulations allows for assignment of 1D bands of B-7AGNRs and confirms high structural quality of aligned B-7AGNRs.

Let us now compare the valence band structures of B-7AGNR and 7AGNRs. Using ARPES maps for aligned 7-AGNRs on Au(788) we have recently determined that the VB maximum is located at 0.87 eV and has an effective electron mass of $m^* \sim 0.4\ m_e$, while the VB–1 edge position is 0.93 eV and an effective mass of VB–1 is $\sim 0.2\ m_e$.[44] Thus the second energy bands (VB–1) for pristine and B-doped systems have equal electron effective masses. Moreover, their energy positions are close to each other. In B-doped 7AGNRs on Au the VB–1 is shifted by 110 meV towards the Fermi level compared to the pristine ribbons.

Substrate effect

To better understand the interaction with the substrate, we performed DFT calculations of the realistic B-7AGNRs/Au(111) system. To fit the periodic boundary conditions for both the ribbon and the substrate, we consider two unit cells of B-7AGNRs. The relaxed geometry is shown in Figure 3 (a). Our analysis of the charge density difference upon the adsorption of B-7AGNR on Au(111), shown in supplementary information (Fig. S4), reveals charge accumulation between the B and Au atoms, that indicates the formation of local, weak chemical bond. This leads to the attraction of B atoms towards the Au substrate and corrugation of the ribbon structure, which explains the angular dependence of the NEXAFS intensity shown earlier. Let us now compare the calculated electronic structures of freestanding and Au-supported B-7AGNRs, which are shown in Figure 3 (b, c). Note that the large super cell of B-7AGNRs/Au(111) result in the twice smaller (folded) BZ. For the freestanding system we also consider the folded band structure. The blue, red and the orange arrows in Figure 3 (b) indicate VB, VB–1 and low lying flat band, respectively. These bands were discussed in the previous section. The green arrow shows the conduction band (CB). The contributions of B and C orbitals to the π-states are denoted by the red and black circles, respectively. When B-7AGNRs are adsorbed on Au(111), hybridization of the VB states (blue arrow in Fig. 3 (c)) with Au states affects the dispersion of this band.

A part is almost degenerate with the parabolic VB–1 up to wavevector of about half the folded BZ length. At larger wavevectors, the band is smeared out over the band gap energy range. This situation renders VB undetectable in ARPES measurements and probably also in STS.[9] The states located closely to the Fermi level are depicted by a green arrow in Figure 3 (c) and originate from the flat CB of freestanding B-7AGNRs *above* the chemical potential (see Fig. 3 (b)). It is challenging to visualize these states in ARPES experiment due to the energy spreading of the CB and strong momentum dependence of the photoemission matrix element for GNRs as discussed before. Nevertheless, the ARPES scan at $k_\perp$ corresponding to the maximum intensity of the CB states reveals an extra ARPES intensity close to the Fermi level (see supplementary information, Fig. S5). This intensity may be attributed to the partially occupied CB, as predicted in the calculations. In this case, the naturally semiconducting B-7AGNRs acquire metallic properties upon adsorption on Au(111) surface.

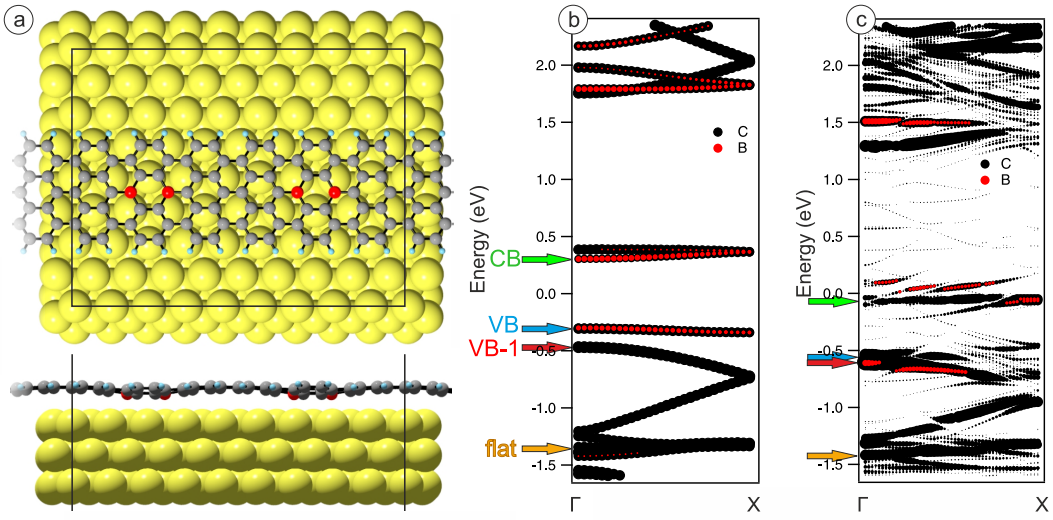

Figure 3: (a) The top and side views of the relaxed structure of large unit cell of B-7AGNRs on Au(111) obtained by DFT. Electronic band structure of (b) freestanding B-7AGNRs and (c) B-7AGNRs on Au(111) in folded BZ (due to the twice larger unit cell). The contributions of B and C π-bands are marked by the black and red circles, respectively. The circle size is proportional to the orbital weights, normalized per amount of atoms in the unit cell. The contribution of B states is 2 times reduced for clarity. The green, blue, red and orange arrows indicate the CB, VB, VB–1 and the low energy flat band, correspondingly.

Let us discuss the impact of the current findings on the fabrication of contacts between

metals and GNRs. Bottom-up synthesized GNRs exhibit Fermi level pinning on Au substrate (that is an asymmetric alignment of CB and VB with a reduced band gap).[45] This effect is typical for metal/organic semiconductor interfaces and junctions, where due to the interface dipole formation a potential barrier for the charge carriers appears.[46–49] Indeed, performance of GNR-based devices suffers from the Schottky barrier.[19–21] Hybridization of electronic states between the metal contact and the 2D material is known to be important for achieving low contact resistance.[50] In B-7AGNRs on gold the VB and CB states becomes energetically extended inside the band gap due to the hybridization, thus eliminating the barrier for electron and hole injection into the nanoribbon. If the B-doped GNR is placed on a lateral Au/insulator/Au interface, so that the central length of the ribbon lies on an insulator and the edges of the ribbon are in contact with gold, then this GNR-based device would simultaneously exhibit low-resistance Ohmic contacts to Au and a field effect with high on/off ratio due to the band gap of the ribbon sitting on the insulating substrate.

Our results on the energy band dispersion and orbital character of B-7AGNRs could also be relevant for understanding of the recent STS data on borylated segments inside 7AGNRs.[16] These experiments revealed high electron transmission for the VB–1 states and no transmission for the the frontier VB states of 7AGNR at the junction. Besides the wavefuncion symmetry arguments,[16] high transparency of the junction may be also related to the fact that the VB–1 in B-7AGNRs has identical effective mass and is close in energy when compared to those of 7AGNRs. The scattering associated to electron transport through the VB of 7AGNRs may be due to the strong hybridization of this band with the Au states in B-doped system.

It is important to mention that the hybridization effect should depend on the substrate material used for on-surface synthesis of B-doped GNRs. Besides gold, bottom-up fabrication of GNRs could be performed on other noble metal surfaces, for example, silver[1,51,52] or cooper.[53–56] The bonding of B atom embedded in sp^2 carbon lattice with cooper is also strong,[57,58] while with silver substrate the attraction of B sites may be weaker since B-Ag

chemical interaction is weaker than B-Au and B-Cu.[59] Thus, we assume that by substrate choice it may be possible to tune interaction of B-doped GNRs with the substrate surface. The realization of unperturbed flat CB and VB, as well as the localized spin centers at the B-7AGNRs/7AGNRs interface,[17] would require freestanding or weakly interacting B-7AGNRs. This might be realized by decoupling of B-7AGNRs from Au, *e.g.* by intercalation of semiconductors underneath the nanoribbons.[60]

Ultra-high vacuum Raman spectroscopy

Organoboron compounds are notoriously known for being sensitive to oxidation.[61] Indeed, we observed oxidation of synthesized B-7AGNRs after air exposure by XPS and Raman spectroscopy (supplementary information, Fig. S1). Therefore, Raman measurements in ambient conditions are inherently unreliable. We have thus employed the UHV Raman technique,[27,41,62] which allows for *in situ* synthesis and Raman measurements keeping the sample always in UHV conditions. Figure 4 (a) shows a comparison of the Raman spectra of B-7AGNRs and pristine 7AGNRs on Au(111). The spectra at the bottom of Figure 4 (a) are obtained for aligned B-7AGNRs on Au(788) with laser polarization along and perpendicular to the alignment direction (that is along the Au(111) terraces). The observed anisotropy of the Raman response of aligned GNRs is a consequence of the optical selection rules and the depolarization effect.[27] The most intense feature in the presented spectra is the G-like mode (in analogy with the G mode of graphene) arising from the C-C bonds vibrations along the ribbon axis. Another important characteristic of the Raman spectra of GNRs is the width-dependent radial-breathing-like mode (RBLM). One can see that the spectral feature of aligned B-7AGNRs on Au(788) closely resemble those for non-aligned ribbons on Au(111). Small differences (for example, the maximum of the G-like peak in aligned ribbons is up-shifted by ~ 5 cm^{-1}) may be related to the inter-ribbon interaction which was also observed in the Raman spectra of densely aligned pristine 7AGNRs.[41] Let us consider the pristine and B-doped ribbons on Au(111). We can immediately see that the Raman spectrum of B-7AGNRs has more peaks compared to the pristine 7AGNRs. This is a consequence of

three times larger unit cell for B-7AGNRs resulting in three times the number of phonon branches, many of which have a nonzero Raman tensor.

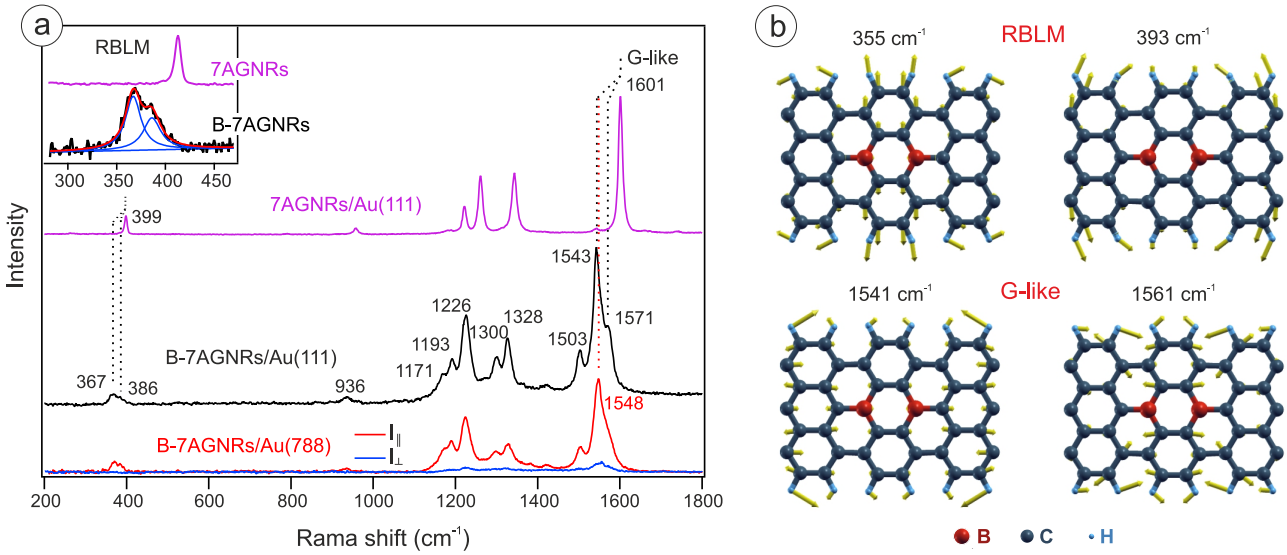

Figure 4: (a) Raman spectra of B-7AGNRs on Au(788) and on Au(111) measured using 532 nm laser inside a UHV chamber. The spectrum of pristine 7AGNRs/Au(111) normalized to the intensity of the G-like band is shown at the top for comparison. Aligned B-7AGNRs/Au(788) were measured with two laser polarizations: along ($I_{\parallel}$) and perpendicular ($I_{\perp}$) to the Au(111) terraces. The inset shows a zoom-in of the region with RBLM modes for 7AGNRs and B-7AGNRs. The vertical dashed lines indicate positions of RBLM and G-like Raman modes in 7AGNRs and B-7AGNRs on Au(111). (b) The calculated eigenvectors of the RBLM and G-like phonon modes appearing in B-7AGNRs.

Interestingly, the periodic incorporation of pairs of B atoms in 7AGNRs leads to a splitting of the prominent RBLM and G-like bands into two components. For the RBLM mode, shown in the inset of Figure 4 (a), we observe a splitting of the peak at 399 cm^{-1} in 7AGNRs into peaks at 367 cm^{-1} and 386 cm^{-1} in B-7AGNRs. Similarly, for the G-like peak (at 1601 cm^{-1} for 7AGNRs) we also observe a shift of the phonon energy to 1543 cm^{-1} and an additional component at higher energies (1571 cm^{-1}). Let us now discuss the origin of this peculiar shifts and splitting. In freestanding sp^2-hybridized carbon lattice substitutional B atoms act as electron acceptors and cause p-type doping. This in turn should lead to the stiffening of the phonon modes, as it was observed for hole doped semiconducting carbon nanotubes.[63] As we uniquely showed by ARPES and DFT, the B-7AGNRs on Au are not

freestanding and the p-doping effect can be ruled out. Moreover our Raman data actually exhibit opposite behavior – softening of the phonons in B-doped nanoribbons.

The larger C–B bond length as compared to the C–C bond[64,65] and resulting lattice strain was assigned to be a reason for the phonon softening in B-doped graphene.[66] This effect should be relevant for B-7AGNRs too. Moreover, our DFT results (like the previous calculations[9]) revealed that the relaxed structure of B-doped 7AGNR has a larger lattice constant (by 1.2%) than one of the pristine nanoribbon, *i.e.* the C–C bond length increases when B atoms are embedded in the backbone of 7AGNR. Indeed, each B atom (having three valence electrons) substitutionally incorporated in sp^2 carbon lattice depletes the *bonding* C π-states by one electron. This leads to the weakening of C–C bonds in B-7AGNRs and the increased spacing between carbon atoms with respect to the pristine system. A phonon softening effect is also well known for graphene, where the lattice expansion may be induced by strain[67] or by electron doping due to the filling of *anti-bonding* π-states.[68] In addition, increased lattice constant can be realized from our ARPES maps (Fig. 2 (e, g)), where the reflexes from parabolic and flat bands are not centered at the edge of the graphene BZ due to the expanded unit cell.

The calculations support the experimental observations. Figure 4 (b) shows the eigenvectors for RBLM and G-like phonon modes in B-7AGNRs. It can be seen that the boron atoms break vibrational degeneracy for atomic displacements in constituent sub-units with and without boron. These two sub-units are the anthracene unit containing only carbon and hydrogen (that is a unit cell of 7AGNRs) and the diboroanthracene with two borons. If the atomic displacements have large amplitude in the anthracene unit, they have a low amplitude in the diboroanthracene unit and vice versa. Let us now look to the frequencies of the vibrational modes for RBLM and G-like phonons in these two structural units. The calculated frequencies for the split RBLM and G-like peaks in B-7AGNRs are also depicted in Figure 4 (b). For the RBLM we get 355 cm^{-1} and 393 cm^{-1} and for the G-like peak we find 1541 cm^{-1} and 1561 cm^{-1}. Both theoretical results are in reasonable agreement to the

experimentally observed Raman frequencies, suggesting that the lattice expansion due to the substitutional incorporation of B atoms is an important contribution. The observed frequency splitting is linked to the vibrations in anthracene and diboroanthracene units which have different force constants. The small difference between the experimental and calculated positions of the G-like and RBLM modes may be related to the corrugation of the ribbon structure and charge redistribution in B-7AGNRs on Au(111). In the supplementary information we show further eigenvectors of Raman active modes for B-7AGNRs.

The spectra in Fig. 4 (a) are normalized to the intensity of the G-like peak, whereas the intensity of 7AGNRs on Au(111) being normalized to the laser power and the accumulation time is ~ 50 times larger than for B-7AGNRs. To see how the intensity and the spectral shape depend on the laser energy, we performed Raman characterization of both pristine and B-doped systems with the red (633 nm) and the blue (442 nm) lasers. The Raman spectra of pristine and B-doped 7AGNR were accumulated in UHV system right after the synthesis. Since the laser light is transmitted in UHV chamber through the air,[41] when the Raman signal of GNRs is weak we could also observe a sharp oxygen peak at 1555 cm^{-1}. The corresponding data shown in Figure 5 demonstrate that compared to the G-like mode, the intensity of the D-like peak in 7-AGNRs is approximately the same with 442 nm laser and about twice larger with 633 nm laser. It is different from graphene, where the intensity ratio of D to G peaks (I^D/I^G) is inversely proportional to the fourth power of excitation energy.[69–71] In contrast to graphene, 1D band structure of GNRs leads to the strongly resonant optical transitions between Van Hove singularities in valence and conduction bands, for example, E_{11} and E_{22} transitions, from VB to CB and from VB–1 to CB+1, correspondingly.[72–74] Here CB+1 is defined by analogy with VB–1 as the second conduction band, counting from the Fermi level. When the excitation energy is off-resonance, the Raman spectroscopy of GNRs is mode-selective, that is some modes may be suppressed, as it was observed for RBLM mode in 9-AGNRs.[5] Moreover, in graphene and carbon nanotubes the D mode originates from a disorder-induced double resonance scattering process. As a result, its frequency strongly

depends on the excitation energy.[75,76] The D-like mode in armchair GNRs can be explained as a first order Raman scattering process, which do not require any defect.[74] Indeed, we observe that the position of the D-like peak for both 7AGNRs (at 1342 cm^{-1}) and B-7AGNRs (at 1226 cm^{-1}) is independent on the laser energy. We also should mention that a small (compared to graphene) dependence of the D-like mode position on the excitation energy was observed in atomically precise cove-shaped GNRs synthesized by solution-based processing, and was assigned to the disorder-induced scattering due to the edge functionalization or defects.[24]

The theory predicts that the optical excitation of the RBLM-like mode for AGNRs have sharp maxima at E_{11} and E_{22} interband direct transition energies.[77] Interestingly, we can detect the RBLM-mode of 7AGNRs within a wide visible light range (Fig. 5 a), although the energy of the red laser (1.96 eV) is slightly lower then the optical band gap of $\sim$ 2.1 eV and the energy of the blue laser (2.81 eV) is higher than the E_{22} transitions of $\sim$ 2.3 eV for 7AGNRs on Au.[78] The RBLM-mode of B-7AGNRs on Au(111) is also visible with the red laser, while for the blue one its intensity is too weak to observe (Fig. 5 b). As can be seen from Table 1, the Raman intensity of the G-like mode for both 7AGNRs and B-7AGNRs is maximal with the green laser (2.33 eV). For pristine system the strong Raman signal with the green laser is known and attributed to the resonant E_{22} transition.[27,78] We assume that for B-7AGNR the green laser should be also close to the E_{22} transition. Indeed, for B-7AGNRs on Au(111) the calculations predicts $\sim$ 2.4 eV separations between VB–1 and CB+1,[8] which also fits to the STS data (revealed a gap of 2.4 eV).[9] The VB–1 and CB+1 states are of a carbon character and, as we demonstrated by ARPES (for VB–1), are not strongly affected by the interaction with gold substrate. Note that due to the metallization of B-7AGNRs on Au, the excitonic effects should be smaller than for pristine 7AGNRs[78] due to the increased screening of many-body interactions, and, consequently, the optical transition energies for B-7AGNRs should be close to the quasi-particle ones. From Table 1 one can see that for B-doped system the G-like mode intensity is much lower, compared to pristine nanoribbons.

For the green laser, this may be in part because of better matching of photon energy to the interband transition in 7AGNRs.[27,78] On the other hand, since for B-7AGNRs the signal is weaker than for 7AGNRs with all three lasers, we suggest that this is associated with a strong interaction with the Au substrate as well. Suppression of the Raman signal is also relevant for graphene, when its π-band is strongly hybridized with the substrate electronic states.[79]

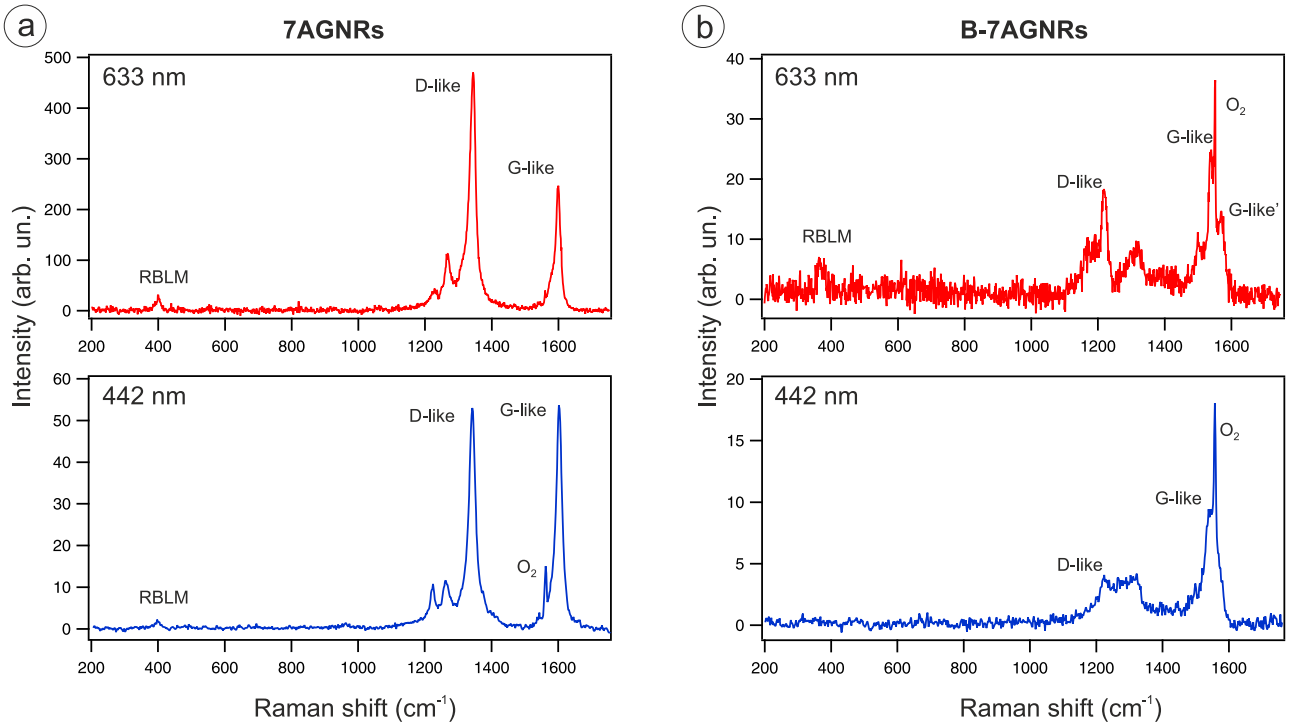

Figure 5: Raman spectra of (a) 7AGNRs and (b) B-7AGNRs on Au(111) measured using 633 nm and 442 nm lasers inside a UHV chamber. The intensity is normalized to the laser power and accumulation time. Besides the GNR-related modes one can see the oxygen peak at 1555 cm^{-1}, due to the passage of the laser through the air before reaching the UHV system. The peak related to the G-like vibrations of diboroanthracene unit in B-7AGNRs (633 nm laser) is labeled as G-like'.

Conclusions

We have performed a comprehensive characterization of the electronic and vibrational properties of atomically precise B-doped GNRs. The substitution of a pair of carbon atoms

Table 1: Experimental Raman intensities (peak values) of G-like mode normalized to the laser power and accumulation time for 7AGNRs ($I^G{}_{7AGNRs}$) and B-7AGNRs ($I^G{}_{B-7AGNRs}$) on Au(111), as well as their ratios. For B-7AGNRs we take the intensity of the G mode vibrations for anthracene unit.

Laser line	$I^G{}_{7AGNRs}$	$I^G{}_{B-7AGNRs}$	$I^G{}_{7AGNRs}/I^G{}_{B-7AGNRs}$
633 nm/1.96 eV	248	24	10.3
532 nm/2.33 eV	14288	278	51.4
442 nm/2.81 eV	53	9	5.9

along the backbone of 7AGNR by boron leads to profound changes in the ARPES and Raman spectra. It is found that B atoms mediate hybridization of B-7AGNR and Au electronic states leading to charge redistribution and periodic corrugation of the ribbon structure. We also found that the VB–1 of 7AGNRs does not change its effective mass and only weakly changes energy if boron substitution is performed. Finally we have overcome the limitations of traditional Raman spectroscopy in air which is unsuitable for the investigation of B-doped GNRs and found that embedded B atoms substantially modify the Raman spectra of 7AGNR. Particularly, we observe the appearance of new characteristic phonon modes, the splitting and the shift of RBLM and G-like modes. Comparing the Raman spectra of pristine and B-doped 7AGNRs we find that both systems have the resonant transition with green (532 nm) laser. Significant suppression of the Raman signal in B-7AGNRs relative to the pristine system for three laser lines (red, green and blue) is attributed to the hybridization of the ribbon and substrate electronic states. The absence of dispersion of the D-like mode with the excitation energy in pristine and B-doped 7AGNRs confirms that the origin of the D-like mode is a single resonance Raman scattering process.

Methods

Synthesis

A monolayer of 9,10-bis(10-bromoanthracen-9-yl)-9,10-dihydro-9,10-diboraanthracene was evaporated onto a clean Au(788) surface from a Knudsen cell. The thickness of deposited organics was calibrated by quartz microbalance and XPS measurements. Hereafter the sample was annealed in order to induce polymerization of the precursor molecules (at 200 °C for 30 min) and dehydrogenation (at 360 °C for 15 min) in order to form B-7AGNRs.[8,9] It is known that the vicinal crystal Au(788) provides directional assembly of 7AGNRs along the narrow ($\sim$ 3.8 nm) terraces with (111) surface.[44,80] Here we used the same approach to align B-7AGNRs. The alignment was probed by polarized Raman spectroscopy.

XPS and NEXAFS

The presented XPS and NEXAFS data were obtained at the German-Russian beamline (RGBL) of the HZB BESSY II synchrotron radiation facility (Berlin, Germany). NEXAFS data were obtained in total electron yield (TEY) mode with energy resolution of 50 meV close to the C K-edge. Preliminary NEXAFS experiments were also performed at the HE-SGM beamline at HZB BESSY II. XPS spectra were measured with photon energy of 330 eV and pass energy of 5 eV in the normal emission geometry. Samples were synthesized in the UHV Raman system and transferred to the synchrotron in UHV suitcase. XPS data indicated no trace of oxygen as confirmed by the absence of an O 1s peak in the scan with 700 eV photon energy. All XPS spectra were calibrated using the Au $4f_{7/2}$ core level at binding energy 84.0 eV.

ARPES

ARPES measurements shown in this work were carried out on samples of B-7AGNRs/Au(788) synthesized *in situ* at the UE112-PGM2 beamline of HZB BESSY II with the 1^2-ARPES endstation. Preliminary ARPES data taken on samples transferred in a UHV suitcase were obtained at the ANTARES beamline of SOLEIL synchrotron[81] and at the I05 beamline of Diamond synchrotron.[82] The presented ARPES spectra were measured using a Scienta R8000 analyzer with a vertical slit, a photon energy of 45 eV and horizontally polarized light. The measurements are performed at room temperature. The (111) terraces of Au(788) crystal,

which determine the direction of B-7AGNR axis, were aligned along the vertical slit of the analyzer. We then modified the photoemission matrix element by rotating the polar angle of the manipulator corresponding to changes in $k_\perp$.[44]

UHV Raman

UHV Raman measurements were performed in the back-scattering geometry using commercial Raman systems (Renishaw) integrated in a homebuilt optical chamber, where the exciting and Raman scattered light were coupled into the vacuum using a long-working distance microscope objective with an NA of ∼0.4. The analysis chamber of the UHV Raman is attached to another chamber where the B-7AGNRs on Au(111) and Au(788) were synthesized. Raman spectra were calibrated using the Si peak at 520.5 cm^{-1} as well as the O_2 peak at 1555 cm^{-1}. The latter appears because the laser passes the air before it enters the UHV system. Polarized Raman measurements were also performed *in situ*.

Photoemission intensity simulation

The photoemission intensity was calculated using the dipole approximation for matrix element and the plane wave as a final state.[26,44] Density-functional-theory (DFT) band structure calculations for the intensity simulation were carried out using the FPLO-14.00-48 (improved version of the previous FPLO code by Koepernik and Eschrig[83]), utilizing the generalized gradient approximation (GGA) to the exchange-correlation potential. The ribbons were assumed freestanding and hydrogen-terminated. A k-point grid of $1 \times 4 \times 1$ was used to sample the BZ. Atomic positions were relaxed until the forces on each atom were less than 10^{-2} eV/Å.

Band structure calculations of B-7AGNRs on Au(111)

The B-7AGNR/Au(111) system was modeled by a slab consisting of five Au atomic layers with a (4×9) in-plane surface unit cell and a vacuum region of at least 18 Å. The *ab initio* results for the system have been obtained with the help of the DFT by employing the GGA for the pseudopotentials generated with the projector augmented wave method (PAW)[84] as implemented in the VASP code.[85–87] For the structural relaxations of the B-doped 7AGNR

and the first Au surface layer, the BZ was sampled by the Γ-point with a threshold value for the calculated forces of 10 meV/Å obtained for a cutoff energy of 500 eV. More details about the electronic structure and the bonding mechanism of B-7AGNR on Au(111) are shown in supplementary information.

Raman calculations

Theoretical calculations were performed with the Quantum-Espresso code[88] using pseudo potentials and plane wave expansion with energy cutoff up to 70 Ry and the Local Density Approximation (LDA) for the exchange correlation potential. The B-7AGNR was simulated using a supercell containing 40 C atoms and 2 B atoms, with more than 10 Å of vacuum along the non-periodic directions. The carbons dangling bonds have been saturated with H atoms ensuring the dynamical stability of the structure.[89] Integration of the charge density was performed using an uniform 411 Monkhorst and Pack grid with fixed occupations. Phonon frequencies were obtained within the linear response theory[88] at the Γ point of the BZ. Non-resonant Raman intensities were calculated using the Placzek approximation[90] as a function of the polarization of the incident and scattered radiation.

Acknowledgements

B.V.S., N.E., A.V.F. and A.G. acknowledge the ERC grant no. 648589 'SUPER-2D', funding from DFG projects CRC 1238 (project A1) and GR 3708/2-1. A.G. ackowledges INST 216/808-1 FUGG and support from the „Quantum Matter and Materials„(QM2) initiative. D.Yu.U. and A.V.F. acknowledge SPbU for research Grant No. 11.65.42.2017 and RFBR (Grant No. 17-02-00427). Research supported by the U.S. Department of Energy (DOE), Office of Science, Basic Energy Sciences (BES), under Award no. DE-SC0010409 (design, synthesis and characterization of molecular building blocks) and the Center for Energy Efficient Electronics Science NSF Award 0939514 (SPM imaging and spectroscopy). The authors gratefully acknowledge the Gauss Centre for Supercomputing (GCS) for providing comput-

ing time through the John von Neumann Institute for Computing (NIC) on the GCS share of the supercomputer JURECA at Jülich Supercomputing Centre (JSC). V.C., S.T. and N.A. gratefully acknowledge financial support from DFG through the CRC 1238 (project C01). This work was supported by French state funds managed by the ANR within the „Investissements d'Avenir„programme under references ANR-17-CE09-0016-05 and ANR-11-IDEX-0004-02, and more specifically within the framework of the Cluster of Excellence MATISSE led by Sorbonne Universités. We thank the Cineca Supercomputing center for the ISCRA computational grant. The research leading to these results has received funding from the European Community's Seventh Framework Programme (FP7/2007-2013) under grant agreement n.312284 (CALIPSO). The Synchrotron SOLEIL is supported by the Centre National de la Recherche Scientifique (CNRS) and the Commissariat à l'Énergie Atomique et aux Énergies Alternatives (CEA), France. We acknowledge Diamond Light Source for time on Beamline I05 under Proposal SI17064. The authors thank HZB BESSY II and the Russian-German Laboratory (RGBL) for the beamtime allocation. This work has been supported by the University of Cologne through the Institutional Strategy of the University of Cologne within the German Excellence Initiative.

References

1. Cai, J.; Ruffieux, P.; Jaafar, R.; Bieri, M.; Braun, T.; Blankenburg, S.; Muoth, M.; Seitsonen, A. P.; Saleh, M.; Feng, X.; Müllen, K.; Fasel, R. Atomically Precise Bottom-up Fabrication of Graphene Nanoribbons. Nature **2010**, 466, 470–473.

2. Chen, Y.-C.; de Oteyza, D. G.; Pedramrazi, Z.; Chen, C.; Fischer, F. R.; Crommie, M. F. Tuning the Band Gap of Graphene Nanoribbons Synthesized from Molecular Precursors. ACS Nano **2013**, 7, 6123–6128.

3. Chen, Y.-C.; Cao, T.; Chen, C.; Pedramrazi, Z.; Haberer, D.; de Oteyza, D. G.; Fischer, F. R.; Louie, S. G.; Crommie, M. F. Molecular Bandgap Engineering of Bottom-up

Synthesized Graphene Nanoribbon Heterojunctions. Nat. Nanotechnol. **2015**, 10, 156–160.

4. Talirz, L.; Ruffieux, P.; Fasel, R. On-Surface Synthesis of Atomically Precise Graphene Nanoribbons. Adv. Mater. **2016**, 28, 6222–6231.

5. Talirz, L.; Sde, H.; Dumslaff, T.; Wang, S.; Sanchez-Valencia, J. R.; Liu, J.; Shinde, P.; Pignedoli, C. A.; Liang, L.; Meunier, V.; Plumb, N. C.; Shi, M.; Feng, X.; Narita, A.; Müllen, K.; Fasel, R.; Ruffieux, P. On-Surface Synthesis and Characterization of 9-Atom Wide Armchair Graphene Nanoribbons. ACS Nano **2017**, 11, 1380–1388.

6. Ma, C.; Liang, L.; Xiao, Z.; Puretzky, A. A.; Hong, K.; Lu, W.; Meunier, V.; Bernholc, J.; Li, A.-P. Seamless Staircase Electrical Contact to Semiconducting Graphene Nanoribbons. Nano Lett. **2017**, 17, 6241–6247.

7. Merino-Díez, N.; Garcia-Lekue, A.; Carbonell-Sanromá, E.; Li, J.; Corso, M.; Colazzo, L.; Sedona, F.; Sánchez-Portal, D.; Pascual, J. I.; de Oteyza, D. G. Width-Dependent Band Gap in Armchair Graphene Nanoribbons Reveals Fermi Level Pinning on Au(111). ACS Nano **2017**, 11, 11661–11668.

8. Cloke, R. R.; Marangoni, T.; Nguyen, G. D.; Joshi, T.; Rizzo, D. J.; Bronner, C.; Cao, T.; Louie, S. G.; Crommie, M. F.; Fischer, F. R. Site-Specific Substitutional Boron Doping of Semiconducting Armchair Graphene Nanoribbons. J. Am. Chem. Soc. **2015**, 137, 8872–8875.

9. Kawai, S.; Saito, S.; Osumi, S.; Yamaguchi, S.; Foster, A. S.; Spijker, P.; Meyer, E. Atomically Controlled Substitutional Boron-doping of Graphene Nanoribbons. Nat. Commun. **2015**, 6, 8098.

10. Usachov, D. Y.; Fedorov, A. V.; Vilkov, O. Y.; Petukhov, A. E.; Rybkin, A. G.; Ernst, A.; Otrokov, M. M.; Chulkov, E. V.; Ogorodnikov, I. I.; Kuznetsov, M. V.; Yashina, L. V.;

Kataev, E. Y.; Erofeevskaya, A. V.; Voroshnin, V. Y.; Adamchuk, V. K.; Laubschat, C.; Vyalikh, D. V. Large-Scale Sublattice Asymmetry in Pure and Boron-Doped Graphene. Nano Lett. **2016**, 16, 4535–4543.

11. Ridley, B. K. Quantum Processes in Semiconductors, 4th ed.; Oxford science publications; Clarendon Press; Oxford University Press, 1999.

12. Levi, A. F. J.; McCall, S. L.; Platzman, P. M. Nonrandom doping and elastic scattering of carriers in semiconductors. Appl. Phys. Lett. **1989**, 54, 940.

13. Kikegawa, N.; Furuya, K. Scattering Reduction due to Electron Wave Interference by Periodic Doping of Impurity Ions in Semiconductors. Phys. B **1996**, 227, 57–60.

14. Liang, L.; Meunier, V. Atomically Precise Graphene Nanoribbon Heterojunctions for Excitonic Solar Cells. J. Phys. Chem. C **2015**, 119, 775–783.

15. Wang, L.; Dong, H.; Guo, Z.; Zhang, L.; Hou, T.; Li, Y. Potential Application of Novel Boron-Doped Graphene Nanoribbon as Oxygen Reduction Reaction Catalyst. J. Phys. Chem. C **2016**, 120, 17427–17434.

16. Carbonell-Sanromà, E.; Brandimarte, P.; Balog, R.; Corso, M.; Kawai, S.; Garcia-Lekue, A.; Saito, S.; Yamaguchi, S.; Meyer, E.; Snchez-Portal, D.; Pascual, J. I. Quantum Dots Embedded in Graphene Nanoribbons by Chemical Substitution. Nano Lett. **2017**, 17, 50–56.

17. Cao, T.; Zhao, F.; Louie, S. G. Topological Phases in Graphene Nanoribbons: Junction States, Spin Centers, and Quantum Spin Chains. Phys. Rev. Lett. **2017**, 119, 076401.

18. Wang, X.; Ouyang, Y.; Li, X.; Wang, H.; Guo, J.; Dai, H. Room-Temperature All-Semiconducting Sub-10-nm Graphene Nanoribbon Field-Effect Transistors. Phys. Rev. Lett. **2008**, 100, 206803.

19. Bennett, P. B.; Pedramrazi, Z.; Madani, A.; Chen, Y.-C.; de Oteyza, D. G.; Chen, C.; Fischer, F. R.; Crommie, M. F.; Bokor, J. Bottom-up Graphene Nanoribbon Field-Effect Transistors. Appl. Phys. Lett. **2013**, 103, 253114.

20. Llinas, J. P.; Fairbrother, A.; Barin, G. B.; Shi, W.; Lee, K.; Wu, S.; Choi, B. Y.; Braganza, R.; Lear, J.; Kau, N.; Choi, W.; Chen, C.; Pedramrazi, Z.; Dumslaff, T.; Narita, A.; Feng, X.; Müllen, K.; Fischer, F.; Zettl, A.; Ruffieux, P. et al. Short-channel Field-effect Transistors with 9-atom and 13-atom wide Graphene Nanoribbons. Nat. Commun. **2017**, 8, 633.

21. Passi, V.; Gahoi, A.; Senkovskiy, B. V.; Haberer, D.; Fischer, F. R.; Grneis, A.; Lemme, M. C. Field-Effect Transistors Based on Networks of Highly Aligned, Chemically Synthesized N = 7 Armchair Graphene Nanoribbons. ACS Appl. Mater. Interfaces **2018**, 10, 9900–9903.

22. Narita, A.; Feng, X.; Hernandez, Y.; Jensen, S. A.; Bonn, M.; Yang, H.; Verzhbitskiy, I. A.; Casiraghi, C.; Hansen, M. R.; Koch, A. H. R.; Fytas, G.; Ivasenko, O.; Li, B.; Mali, K. S.; Balandina, T.; Mahesh, S.; Feyter, S. D.; Müllen, K. Synthesis of Structurally Well-defined and Liquid-phase-processable Graphene Nanoribbons. Nat. Chem. **2014**, 6, 126132.

23. Vo, T. H.; Shekhirev, M.; Kunkel, D. A.; Orange, F.; Guinel, M. J.-F.; Enders, A.; Sinitskii, A. Bottom-up Solution Synthesis of Narrow Nitrogen-doped Graphene Nanoribbons. Chem. Commun. **2014**, 50, 4172–4174.

24. Verzhbitskiy, I. A.; Corato, M. D.; Ruini, A.; Molinari, E.; Narita, A.; Hu, Y.; Schwab, M. G.; Bruna, M.; Yoon, D.; Milana, S.; Feng, X.; Müllen, K.; Ferrari, A. C.; Casiraghi, C.; Prezzi, D. Raman Fingerprints of Atomically Precise Graphene Nanoribbons. Nano Lett. **2016**, 16, 3442–3447.

25. Pour, M. M.; Lashkov, A.; Radocea, A.; Liu, X.; Sun, T.; Lipatov, A.; Korlacki, R. A.;

Shekhirev, M.; Aluru, N. R.; Lyding, J. W.; Sysoev, V.; Sinitskii, A. Laterally Extended Atomically Precise Graphene Nanoribbons with Improved Electrical Conductivity for Efficient Gas Sensing. Nat. Commun. **2017**, 8, 820.

26. Senkovskiy, B. V.; Haberer, D.; Usachov, D. Y.; Fedorov, A. V.; Ehlen, N.; Hell, M.; A., R. D.; Fischer, F. R.; Grüneis, A. Spectroscopic Characterization of N=9 Armchair Graphene Nanoribbons. Phys. Status Solidi RRL **2017**, 11, 1700157.

27. Senkovskiy, B. V.; Pfeiffer, M.; Alavi, S. K.; Bliesener, A.; Zhu, J.; Michel, S.; Fedorov, A. V.; German, R.; Hertel, D.; Haberer, D.; Petaccia, L.; Fischer, F. R.; Meerholz, K.; van Loosdrecht, P. H. M.; Lindfors, K.; Grüneis, A. Making Graphene Nanoribbons Photoluminescent. Nano Lett. **2017**, 17, 4029–4037.

28. Bronner, C.; Stremlau, S.; Gille, M.; Braue, F.; Haase, A.; Hecht, S.; Tegeder, P. Aligning the Band Gap of Graphene Nanoribbons by Monomer Doping. Angew. Chem. Int. Ed. **2013**, 52, 4422–4425.

29. Cai, J.; Pignedoli, C. A.; Talirz, L.; Ruffieux, P.; Söde, H.; Liang, L.; Meunier, V.; Berger, R.; Li, R.; Feng, X.; Müllen, K.; Fasel, R. Graphene Nanoribbon Heterojunctions. Nat. Nanotechnol. **2014**, 9, 896–900.

30. Zhang, Y.; Zhang, Y.; Li, G.; Lu, J.; Lin, X.; Du, S.; Berger, R.; Feng, X.; Mllen, K.; Gao, H.-J. Direct Visualization of Atomically Precise Nitrogen-doped Graphene Nanoribbons. Appl. Phys. Lett. **2014**, 105, 023101.

31. Nguyen, G. D.; Toma, F. M.; Cao, T.; Pedramrazi, Z.; Chen, C.; Rizzo, D. J.; Joshi, T.; Bronner, C.; Chen, Y.-C.; Favaro, M.; Louie, S. G.; Fischer, F. R.; Crommie, M. F. Bottom-Up Synthesis of N = 13 Sulfur-Doped Graphene Nanoribbons. J. Phys. Chem. C **2016**, 120, 2684–2687.

32. Ruffieux, P.; Wang, S.; Yang, B.; Sànchez-Sànchez, C.; Liu, J.; Dienel, T.; Talirz, L.; Shinde, P.; Pignedoli, C. A.; Passerone, D.; Dumslaff, T.; Feng, X.; Müllen, K.; Fasel, R.

On-surface Synthesis of Graphene Nanoribbons with Zigzag Edge Topology. Nature **2016**, 531, 489.

33. Basagni, A.; Vasseur, G.; Pignedoli, C. A.; Vilas-Varela, M.; Pea, D.; Nicolas, L.; Vitali, L.; Lobo-Checa, J.; de Oteyza, D. G.; Sedona, F.; Casarin, M.; Ortega, J. E.; Sambi, M. Tunable Band Alignment with Unperturbed Carrier Mobility of On-Surface Synthesized Organic Semiconducting Wires. ACS Nano **2016**, 10, 2644–2651.

34. Carbonell-Sanromà, E.; Hieulle, J.; Vilas-Varela, M.; Brandimarte, P.; Iraola, M.; Barragàn, A.; Li, J.; Abadia, M.; Corso, M.; Snchez-Portal, D.; Peña, D.; Pascual, J. I. Doping of Graphene Nanoribbons via Functional Group Edge Modification. ACS Nano **2017**, 11, 7355–7361.

35. Nguyen, G. D.; Tsai, H.-Z.; Omrani, A. A.; Marangoni, T.; Wu, M.; Rizzo, D. J.; Rodgers, G. F.; Cloke, R. R.; Durr, R. A.; Sakai, Y.; Liou, F.; Aikawa, A. S.; Chelikowsky, J. R.; Louie, S. G.; Fischer, F. R.; Crommie, M. F. Atomically Precise Graphene Nanoribbon Heterojunctions from a Single Molecular Precursor. Nat. Nanotechnol. **2017**, 12, 10771082.

36. Zhang, Y.-F.; Zhang, Y.; Li, G.; Lu, J.; Que, Y.; Chen, H.; Berger, R.; Feng, X.; Müllen, K.; Lin, X.; Zhang, Y.-Y.; Du, S.; Pantelides, S. T.; Gao, H.-J. Sulfur-doped Graphene Nanoribbons with a Sequence of Distinct Band Gaps. Nano Res. **2017**, 10, 3377–3384.

37. Durr, R. A.; Haberer, D.; Lee, Y.-L.; Blackwell, R.; Kalayjian, A. M.; Marangoni, T.; Ihm, J.; Louie, S. G.; Fischer, F. R. Orbitally Matched Edge-Doping in Graphene Nanoribbons. J. Am. Chem. Soc. **2018**, 140, 807–813.

38. Bronner, C.; Durr, R. A.; Rizzo, D. J.; Lee, Y.-L.; Marangoni, T.; Kalayjian, A. M.; Rodriguez, H.; Zhao, W.; Louie, S. G.; Fischer, F. R.; Crommie, M. F. Hierarchical

On-Surface Synthesis of Graphene Nanoribbon Heterojunctions. ACS Nano **2018**, 12, 2193–2200.

39. Kawai, S.; Nakatsuka, S.; Hatakeyama, T.; Pawlak, R.; Meier, T.; Tracey, J.; Meyer, E.; Foster, A. S. Multiple Heteroatom Substitution to Graphene Nanoribbon. Sci. Adv. **2018**, 4.

40. Slota, M.; Keerthi, A.; Myers, W. K.; Tretyakov, E.; Baumgarten, M.; Ardavan, A.; Sadeghi, H.; Lambert, C. J.; Narita, A.; Müllen, K.; Bogani, L. Magnetic edge states and coherent manipulation of graphene nanoribbons. Nature **2018**, 557, 691695.

41. Senkovskiy, B. V.; Fedorov, A. V.; Haberer, D.; Farjam, M.; Simonov, K. A.; Preobrajenski, A. B.; Mårtensson, N.; Atodiresei, N.; Caciuc, V.; Blügel, S.; Rosch, A.; Verbitskiy, N. I.; Hell, M.; Evtushinsky, D. V.; German, R.; Marangoni, T.; van Loosdrecht, P. H. M.; Fischer, F. R.; Grüneis, A. Semiconductor-to-Metal Transition and Quasiparticle Renormalization in Doped Graphene Nanoribbons. Adv. Electron. Mater. **2017**, 3, 1600490.

42. Usachov, D. Y.; Fedorov, A. V.; Petukhov, A. E.; Vilkov, O. Y.; Rybkin, A. G.; Otrokov, M. M.; Arnau, A.; Chulkov, E. V.; Yashina, L. V.; Farjam, M.; Adamchuk, V. K.; Senkovskiy, B. V.; Laubschat, C.; Vyalikh, D. V. Epitaxial B-Graphene: Large-Scale Growth and Atomic Structure. ACS Nano **2015**, 9, 7314–7322.

43. Lv, R.; Chen, G.; Li, Q.; McCreary, A.; Botello-Méndez, A.; Morozov, S. V.; Liang, L.; Declerck, X.; Perea-López, N.; Cullen, D. A.; Feng, S.; Elías, A. L.; Cruz-Silva, R.; Fujisawa, K.; Endo, M.; Kang, F.; Charlier, J.-C.; Meunier, V.; Pan, M.; Harutyunyan, A. R. et al. Ultrasensitive Gas Detection of Large-area Boron-doped Graphene. Proc. Natl. Acad. Sci. U. S. A. **2015**, 112, 14527–14532.

44. Senkovskiy, B. V.; Usachov, D. Y.; Fedorov, A. V.; Haberer, D.; ; Ehlen, N.; Fischer, F. R.; Grüneis, A. Finding the Hidden Valence Band of N=7 Armchair Graphene

Nanoribbons with Angle-Resolved Photoemission Spectroscopy. 2D Mater. **2018**, 5, 035007.

45. Merino-Díez, N.; Garcia-Lekue, A.; Carbonell-Sanromá, E.; Li, J.; Corso, M.; Colazzo, L.; Sedona, F.; Sánchez-Portal, D.; Pascual, J. I.; de Oteyza, D. G. Width-Dependent Band Gap in Armchair Graphene Nanoribbons Reveals Fermi Level Pinning on Au(111). ACS Nano **2017**, 11, 11661–11668.

46. Hisao, I.; Kiyoshi, S.; Eisuke, I.; Kazuhiko, S. Energy Level Alignment and Interfacial Electronic Structures at Organic/Metal and Organic/Organic Interfaces. Adv. Mater. **2015**, 11, 605–625.

47. Hwang, J.; Wan, A.; Kahn, A. Energetics of Metalorganic Interfaces: New Experiments and Assessment of the Field. Mater. Sci. Eng., R **2009**, 64, 1–31.

48. Heimel, G.; Duhm, S.; Salzmann, I.; Gerlach, A.; Strozecka, A.; Niederhausen, J.; Bürker, C.; Hosokai, T.; Fernandez-Torrente, I.; Schulze, G.; Winkler, S.; Wilke, A.; Schlesinger, R.; Frisch, J.; Bröker, B.; Vollmer, A.; Detlefs, B.; Pflaum, J.; Kera, S.; Franke, K. J. et al. Charged and Metallic Molecular Monolayers through Surface-induced Aromatic Atabilization. Nat. Chem. **2013**, 5, 187194.

49. Elizabeth, G.; Patrizia, B.; Afaf, E.; Enrique, O. J.; de Oteyza Dimas G., MultiComponent Organic Layers on Metal Substrates. Adv. Mater. **2015**, 28, 1340–1368.

50. Allain, A.; Kang, J.; Banerjee, K.; Kis, A. Electrical contacts to two-dimensional semiconductors. Nat. Mater. **2015**, 14, 11951205.

51. Huang, H.; Wei, D.; Sun, J.; Wong, S. L.; Feng, Y. P.; Neto, A. H. C.; Wee, A. T. S. Spatially Resolved Electronic Structures of Atomically Precise Armchair Graphene Nanoribbons. Sci. Rep. **2012**, 2, 983.

52. de Oteyza, D. G.; García-Lekue, A.; Vilas-Varela, M.; Merino-Díez, N.; Carbonell-Sanromá, E.; Corso, M.; Vasseur, G.; Rogero, C.; Guitián, E.; Pascual, J. I.; Ortega, J. E.; Wakayama, Y.; Peña, D. Substrate-Independent Growth of Atomically Precise Chiral Graphene Nanoribbons. ACS Nano **2016**, 10, 9000–9008.

53. Simonov, K. A.; Vinogradov, N. A.; Vinogradov, A. S.; Generalov, A. V.; Zagrebina, E. M.; Mårtensson, N.; Cafolla, A. A.; Carpy, T.; Cunniffe, J. P.; Preobrajenski, A. B. Effect of Substrate Chemistry on the Bottom-Up Fabrication of Graphene Nanoribbons: Combined Core-Level Spectroscopy and STM Study. J. Phys. Chem. C **2014**, 118, 12532–12540.

54. Sánchez-Sánchez, C.; Dienel, T.; Deniz, O.; Ruffieux, P.; Berger, R.; Feng, X.; Müllen, K.; Fasel, R. Purely Armchair or Partially Chiral: Noncontact Atomic Force Microscopy Characterization of Dibromo-Bianthryl-Based Graphene Nanoribbons Grown on Cu(111). ACS Nano **2016**, 10, 8006–8011.

55. Schulz, F.; Jacobse, P. H.; Canova, F. F.; van der Lit, J.; Gao, D. Z.; van den Hoogenband, A.; Han, P.; Klein Gebbink, R. J.; Moret, M.-E.; Joensuu, P. M.; Swart, I.; Liljeroth, P. Precursor Geometry Determines the Growth Mechanism in Graphene Nanoribbons. J. Phys. Chem. C **2017**, 121, 2896–2904.

56. Simonov, K. A.; Generalov, A. V.; Vinogradov, A. S.; Svirskiy, G. I.; Cafolla, A. A.; McGuinness, C.; Taketsugu, T.; Lyalin, A.; Preobrajenski, N. M. . A. B. Synthesis of Armchair Graphene Nanoribbons from the 10,10′-dibromo-9,9′-bianthracene Molecules on Ag(111): the Role of Organometallic Intermediates. Sci. Rep. **2018**, 8, 3506.

57. Zhao, L.; Levendorf, M.; Goncher, S.; Schiros, T.; Plov, L.; Zabet-Khosousi, A.; Rim, K. T.; Gutirrez, C.; Nordlund, D.; Jaye, C.; Hybertsen, M.; Reichman, D.; Flynn, G. W.; Park, J.; Pasupathy, A. N. Local Atomic and Electronic Structure of Boron Chemical Doping in Monolayer Graphene. Nano Lett. **2013**, 13, 4659–4665.

58. Ferrighi, L.; Trioni, M. I.; Di Valentin, C. Boron-Doped, Nitrogen-Doped, and Codoped Graphene on Cu(111): A DFT + vdW Study. J. Phys. Chem. C **2015**, 119, 6056–6064.

59. Matkovich, V. I. Boron and Refractory Borides; Springer-Verlag Berlin Heidelberg, 1977.

60. Deniz, O.; Sánchez-Sánchez, C.; Dumslaff, T.; Feng, X.; Narita, A.; Müllen, K.; Kharche, N.; Meunier, V.; Fasel, R.; Ruffieux, P. Revealing the Electronic Structure of Silicon Intercalated Armchair Graphene Nanoribbons by Scanning Tunneling Spectroscopy. Nano Lett. **2017**, 17, 2197–2203.

61. Jäkle, F. Advances in the Synthesis of Organoborane Polymers for Optical, Electronic, and Sensory Applications. Chem. Rev. **2010**, 7, 39854022.

62. Grüneis, A.; Senkovskiy, B.; Fedorov, A.; Hell, M.; Michel, S. Encyclopedia of Interfacial Chemistry; Elsevier, 2018; pp 367–374.

63. Das, A.; Sood, A. K. Renormalization of the Phonon Spectrum in Semiconducting Single-walled Carbon Nanotubes Studied by Raman Spectroscopy. Phys. Rev. B **2009**, 79, 235429.

64. Chuandong, D.; Shohei, S.; Kyohei, M.; Ichiro, H.; Shigehiro, Y. A Boron-Containing PAH as a Substructure of Boron-Doped Graphene. Angew. Chem. Int. Ed. **2012**, 51, 12206–12210.

65. Choudhuri, I.; Patra, N.; Mahata, A.; Ahuja, R.; Pathak, B. BNGraphene: Highly Sensitive and Selective Gas Sensor. J. Phys. Chem. C **2015**, 119, 24827–24836.

66. Kim, Y. A.; Fujisawa, K.; Muramatsu, H.; Hayashi, T.; Endo, M.; Fujimori, T.; Kaneko, K.; Terrones, M.; Behrends, J.; Eckmann, A.; Casiraghi, C.; Novoselov, K. S.; Saito, R.; Dresselhaus, M. S. Raman Spectroscopy of Boron-Doped Single-Layer Graphene. ACS Nano **2012**, 6, 6293–6300.

67. Mohiuddin, T. M. G.; Lombardo, A.; Nair, R. R.; Bonetti, A.; Savini, G.; Jalil, R.; Bonini, N.; Basko, D. M.; Galiotis, C.; Marzari, N.; Novoselov, K. S.; Geim, A. K.; Ferrari, A. C. Uniaxial Strain in Graphene by Raman Spectroscopy: G Peak Splitting, Grüneisen Parameters, and Sample Orientation. Phys. Rev. B **2009**, 79, 205433.

68. Lazzeri, M.; Mauri, F. Nonadiabatic Kohn Anomaly in a Doped Graphene Monolayer. Phys. Rev. Lett. **2006**, 97, 266407.

69. Cançado, L. G.; Takai, K.; Enoki, T.; Endo, M.; Kim, Y. A.; Mizusaki, H.; Jorio, A.; Coelho, L. N.; Magalhães Paniago, R.; Pimenta, M. A. General Equation for the Determination of the Crystallite Size La of Nanographite by Raman Spectroscopy. Appl. Phys. Lett. **2006**, 88, 163106.

70. Sato, K.; Saito, R.; Oyama, Y.; Jiang, J.; Cançado, L.; Pimenta, M.; Jorio, A.; Samsonidze, G.; Dresselhaus, G.; Dresselhaus, M. D-band Raman Intensity of Graphitic Materials as a Function of Laser Energy and Crystallite Size. Chem. Phys. Lett. **2006**, 427, 117 – 121.

71. Cançado, L. G.; Jorio, A.; Pimenta, M. A. Measuring the Absolute Raman Cross Section of Nanographites as a Function of Laser Energy and Crystallite Size. Phys. Rev. B **2007**, 76, 064304.

72. Li, Y.; Marvin, L. C.; Steven, G. L. Excitonic Effects in the Optical Spectra of Graphene Nanoribbons. Nano Lett. **2007**, 7, 3112–3115.

73. Prezzi, D.; Varsano, D.; Ruini, A.; Marini, A.; Molinari, E. Optical Properties of Graphene Nanoribbons: The Role of Many-body Effects. Phys. Rev. B **2008**, 77, 041404.

74. Sasaki, K.-i.; Kato, K.; Tokura, Y.; Suzuki, S.; Sogawa, T. Pseudospin for Raman D Band in Armchair Graphene Nanoribbons. Phys. Rev. B **2012**, 85, 075437.

75. Thomsen, C.; Reich, S. Double Resonant Raman Scattering in Graphite. Phys. Rev. Lett. **2000**, 85, 5214–5217.

76. Souza, M.; Jorio, A.; Fantini, C.; Neves, B. R. A.; Pimenta, M. A.; Saito, R.; Ismach, A.; Joselevich, E.; Brar, V. W.; Samsonidze, G. G.; Dresselhaus, G.; Dresselhaus, M. S. Single- and Double-resonance Raman *G*-band Processes in Carbon Nanotubes. Phys. Rev. B **2004**, 69, 241403.

77. Sanders, G. D.; Nugraha, A. R. T.; Saito, R.; Stanton, C. J. Coherent Radial-breathing-like Phonons in Graphene Nanoribbons. Phys. Rev. B **2012**, 85, 205401.

78. Denk, R.; Hohage, M.; Zeppenfeld, P.; Cai, J.; Pignedoli, C. A.; Söde, H.; Fasel, R.; Feng, X.; Müllen, K.; Wang, S.; Prezzi, D.; Ferretti, A.; Ruini, A.; Molinari, E.; Ruffieux, P. Exciton-dominated Optical Response of Ultra-narrow Graphene Nanoribbons. Nat. Commun. **2014**, 5, 4253.

79. Usachov, D. Y.; Davydov, V. Y.; Levitskii, V. S.; Shevelev, V. O.; Marchenko, D.; Senkovskiy, B. V.; Vilkov, O. Y.; Rybkin, A. G.; Yashina, L. V.; Chulkov, E. V.; Sklyadneva, I. Y.; Heid, R.; Bohnen, K.-P.; Laubschat, C.; Vyalikh, D. V. Raman Spectroscopy of Lattice-Matched Graphene on Strongly Interacting Metal Surfaces. ACS Nano **2017**, 11, 6336–6345.

80. Linden, S.; Zhong, D.; Timmer, A.; Aghdassi, N.; Franke, J. H.; Zhang, H.; Feng, X.; Müllen, K.; Fuchs, H.; Chi, L.; Zacharias, H. Electronic Structure of Spatially Aligned Graphene Nanoribbons on Au(788). Phys. Rev. Lett. **2012**, 108, 216801.

81. Avila, J. e.; Asensio, M. C. First NanoARPES User Facility Available at SOLEIL: An Innovative and Powerful Tool for Studying Advanced Materials. Synchrotron Radiat. News **2014**, 27, 24–30.

82. Hoesch, M.; Kim, T. K.; Dudin, P.; Wang, H.; Scott, S.; Harris, P.; Patel, S.; Matthews, M.; Hawkins, D.; Alcock, S. G.; Richter, T.; Mudd, J. J.; Basham, M.;

Pratt, L.; Leicester, P.; Longhi, E. C.; Tamai, A.; Baumberger, F. A Facility for the Analysis of the Electronic Structures of Solids and Their Surfaces by Synchrotron Radiation Photoelectron Spectroscopy. Rev. Sci. Instrum. **2017**, 88, 013106.

83. Koepernik, K.; Eschrig, H. Full-potential Nonorthogonal Local-orbital Minimum-basis Band-structure Scheme. Phys. Rev. B **1999**, 59, 1743–1757.

84. Blöchl, P. E. Projector augmented-wave method. Phys. Rev. B **1994**, 50, 17953–17979.

85. Kresse, G.; Hafner, J. Ab Initio Molecular Dynamics for Liquid Metals. Phys. Rev. B **1993**, 47, 558–561.

86. Kresse, G.; Furthmüller, J. Efficient Iterative Schemes for *ab initio* Total-energy Calculations using a Plane-wave Basis Set. Phys. Rev. B **1996**, 54, 11169–11186.

87. Kresse, G.; Joubert, D. From Ultrasoft Pseudopotentials to the Projector Augmented-wave Method. Phys. Rev. B **1999**, 59, 1758–1775.

88. Giannozzi, P.; Baroni, S.; Bonini, N.; Calandra, M.; Car, R.; Cavazzoni, C.; Ceresoli, D.; Chiarotti, G. L.; Cococcioni, M.; Dabo, I.; Corso, A. D.; de Gironcoli, S.; Fabris, S.; Fratesi, G.; Gebauer, R.; Gerstmann, U.; Gougoussis, C.; Kokalj, A.; Lazzeri, M.; Martin-Samos, L. et al. QUANTUM ESPRESSO: a Modular and Open-source Software Project for Quantum Simulations of Materials. J. Phys. Condens. Matter **2009**, 21, 395502.

89. Tan, Z. W.; Wang, J.-S.; Gan, C. K. First-Principles Study of Heat Transport Properties of Graphene Nanoribbons. Nano Lett. **2011**, 11, 214–219.

90. Lazzeri, M.; Mauri, F. First-Principles Calculation of Vibrational Raman Spectra in Large Systems: Signature of Small Rings in Crystalline SiO_2. Phys. Rev. Lett. **2003**, 90, 036401.